

Selenite Sorption on Hydrated CEM-V/A Cement in the Presence of Steel Corrosion Products: Redox vs Nonredox Sorption

Bin Ma,* Alejandro Fernandez-Martinez,* Kaifeng Wang, Benoît Madé, Pierre Hénocq, Delphine Tisserand, Sarah Bureau, and Laurent Charlet



Cite This: <https://dx.doi.org/10.1021/acs.est.9b06876>



Read Online

ACCESS |



Metrics & More

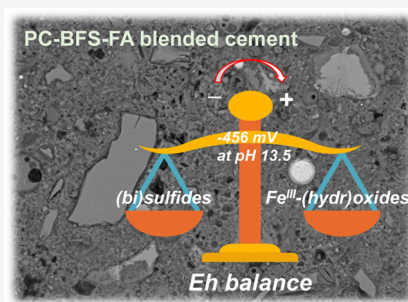


Article Recommendations



Supporting Information

ABSTRACT: Reinforced cementitious structures in nuclear waste repositories will act as barriers that limit the mobility of radionuclides (RNs) in case of eventual leakage. CEM-V/A cement, a ternary blended cement with blast furnace slag (BFS) and fly ash (FA), could be qualified and used in nuclear waste disposal. Chemical interactions between the cement and RNs are critical but not completely understood. Here, we combined wet chemistry methods, synchrotron-based X-ray techniques, and thermodynamic modeling to explore redox interactions and nonredox sorption processes in simulated steel-reinforced CEM-V/A hydration systems using selenite as a molecular probe. Among all of the steel corrosion products analyzed, only the addition of Fe^0 can obviously enhance the reducing ability of cement toward selenite. In comparison, steel corrosion products showed stronger reducing power in the absence of cement hydrates. Selenium K-edge X-ray absorption spectroscopy (XAS) revealed that selenite immobilization mechanisms included nonredox inner-/outer-sphere complexations and reductive precipitations of FeSe and/or Se(0) . Importantly, the hydrated pristine cement showed a good reducing ability, driven by ferrous phases and (bi)sulfides (as shown by sulfur K-edge XAS) originated from BFS and FA. The overall redox potential imposed by hydrated CEM-V/A was determined, hinting to a redox shift in underground cementitious structures.



1. INTRODUCTION

Geological storage in clay-rich host rocks is foreseen in France for radioactive waste.^{1,2} In the repositories, reinforced cementitious materials are used for waste matrix, canisters, backfill, and tunnel support, which are considered as barriers inhibiting the mobility of radionuclides (RNs) in case of eventual leakage. The selection of a suitable type of cement is critical. The anticipated cement should be adequate for the subterranean work in the harsh repository environment, be friendly in CO_2 emission, and certainly be effective for the immobilization of RNs. CEM-V/A cement, a ternary blended cement consisting of 50% Portland cement (PC), 25% blast furnace slag (BFS, may contain sulfides), and 25% fly ash (FA), could be qualified and be expected to be used in French nuclear waste disposal.^{3,4}

In a reinforced cementitious system, cement hydrates and steel corrosion products are elements with a large potential to immobilize RNs. Ordinary Portland cement hydrates typically include calcium silicate hydrates (C–S–H, the major component in hydrated cement),⁵ two series of aluminoferrites—ettringite^{6,7} and AFm phases,^{8,9} and portlandite. Numerous studies have reported the sorption behavior of RNs on cement hydration products.^{10–12} For instance, redox-sensitive selenium-79 (^{79}Se , $t_{1/2} = 3.27(8) \times 10^5$ years)¹³ is considered as one of the few radionuclides that can dominate the ultimate biosphere exposure.¹⁴ Under Eh–pH conditions

typical of the oxidative alteration of spent nuclear fuel, oxidized Se species of $\text{Se(IV)}/\text{Se(VI)}$ are the dominant aqueous species.¹⁵ Sorption of Se oxyanions, such as selenite (SeO_3^{2-}) and selenate (SeO_4^{2-}), has attracted extensive attention, as they are highly mobile. Their reductive precipitation into insoluble Se(0) , Se(-I) , Se(-II) is considered as the most effective way to immobilize ^{79}Se .¹⁶ Previous reports show that AFm phases are potential candidates for the retention of $\text{SeO}_3^{2-}/\text{SeO}_4^{2-}$.^{17–19} Ettringite and C–S–H also show a good affinity to SeO_3^{2-} .^{18,19} On the other hand, corrosion of the steel embedded in concrete could result in white rust (Fe(OH)_2), magnetite (Fe_3O_4), goethite ($\alpha\text{-FeOOH}$), and hematite ($\alpha\text{-Fe}_2\text{O}_3$),²⁰ going along a cross section from the inner to outer level. Fe^0 and its corrosion products can also immobilize Se(IV) through reductive precipitation and surface adsorption (inner-sphere complexation in most cases).^{21,22} Furthermore, most CEM-V/A cement probably contains Fe-(oxyhydr)oxides and metal (bi)sulfides, which originate from the blended BFS and FA, and which are effective for the removal of RNs. As previously reported, under acidic to slightly alkaline conditions, Fe^0

Received: November 13, 2019

Revised: January 21, 2020

Accepted: January 23, 2020

Published: January 23, 2020

(bi)sulfides (e.g., pyrite,²³ pyrrhotite,²⁴ greigite,^{16,25} and mackinawite²⁶) are able to efficiently immobilize Se(IV), resulting in Se(0), FeSe, and/or FeSe₂ reduction products. The way how these minerals would interact with Se(IV) after going through “in situ” cement hydration is critical.

Reinforced ternary blended cement is a complex system when considered as an entire chemical barrier for RNs. Under the combined action of various potential adsorbents, different sorption sites would compete to attract RNs, resulting in nonredox and redox sorption. In this study, we aimed to investigate the redox-sensitive RN sorption behavior in the simulated hydrated environments (hyperalkaline and anaerobic conditions) of reinforced blended cement by means of a combination of wet chemistry methods, synchrotron-based X-ray spectroscopic analysis, and thermodynamic modeling. SeO₃²⁻, the analogue of ⁷⁹SeO₃²⁻, was employed as a probe molecule to detect nonredox and redox sorption sites present in hydrated CEM-V/A cement. Fe⁰ and various Fe-(oxyhydr)-oxides couples were introduced to simulate the presence of steel corrosion interfaces. Although corroded steel has big differences with the nanosized Fe products in ductility, hardness, and melting points, its chemical properties (e.g., the exhibited redox potentials) should have quite high similarities. Compared to that of corroded bulk steel, the high specific surface of the Fe products should accelerate reaching redox equilibrium. We expected that SeO₃²⁻ would be immobilized by different nonredox and redox sorption sites with a certain preferential order that could be ascertained by spectroscopic and thermodynamic investigations. This work provides a detailed description of the redox reaction products present in the system and a better understanding of the redox potential imposed by various reduced phases in the blended cement.

2. MATERIALS AND METHODS

2.1. Materials and Chemicals. All of the chemicals used for synthesis and the stock solutions, including Fe salts (e.g., FeCl₂·4H₂O, FeCl₃·6H₂O, and Fe(NO₃)₃·9H₂O) and the ⁷⁹Se RN anionic analogue Na₂SeO₃·5H₂O, were purchased from Sigma-Aldrich and were of analytical grade. Their containers were opened for the first time before use in a glovebox. The Rombas's CEM V/A (Calcia) cement was received from French Alternative Energies and Atomic Energy Commission (CEA). A detailed chemical composition and mineralogical evolution during hydration is given in a recent study.³ The corresponding synthetic cement pore water (CPW) and all of the Fe products, including nano-zero-valent iron (NZVI), magnetite, hematite, and goethite, were synthesized as described in our previous work.²² The pH value of CPW was ~13.5, and its composition is given in Table S1. All experiments were performed in a N₂-filled glovebox (O₂ < 2 ppm, using NaOH as the CO₂ trap) to prevent oxidation and the possible CO₂ contamination. Boiled and argon-degassed Milli-Q water (18.2 MΩ·cm) was used for all of the reactions.

2.2. Preparation of Hydrated Fe-Bearing Cement Powders. Seven types of hydrated Fe-bearing cement powders, also including the blank hydrated CEM-V/A cement (HCEM-V), were prepared. Of them, three types, including NZVI-bearing cement (C-NZVI), magnetite–hematite coupling cement (C-M/H), and magnetite–goethite coupling cement (C-M/G), were produced with the aim of simulating corroded steel interfaces in hydrated cement. A 4:1 mass ratio of CEM-V/A cement powder to total Fe element content was

used, with each two Fe-(hydr)oxides pairs added in equal proportions. Three other types consisted of hydrated cement phases with the three Fe-(hydr)oxides introduced individually, named C-Mag, C-Hem, and C-Goe. The water-to-cement (W/C) ratio was set to 0.4, and all of the components were mixed until a homogeneous sample was formed. After 2 days of cement setting, the cement paste was covered by degassed ultrapure water for 28 days. Subsequently, the cement cores were extracted, dried under vacuum to stop hydration, ground into a powder with an agate mortar, sieved through 63 μm sieves, and then stored in a glovebox. All of the preparation procedures were performed under highly pure N₂ (>99.995%) protection.

2.3. Wet Chemistry Experiments. HCEM-V equilibrium kinetics with CPW, sorption kinetics of SeO₃²⁻ on HCEM-V, and batch sorption of SeO₃²⁻ on all of the seven types of hydrated Fe-bearing cement particles were investigated at 25 °C in a N₂-filled glovebox. An identical solid-to-liquid (S/L) ratio was fixed as 10 g L⁻¹, and an initial Se concentration of 2 × 10⁻⁴ M was applied. During the reaction, all of the reactors were constantly placed in an end-over-end shaker. For the kinetic study, at each defined time interval, a 2 mL aliquot of the suspension was sampled by filtration through a 0.22 μm pore size membrane filter. In batch sorption experiments, Se was introduced after the cement powders were equilibrated with CPW for 2 days. After equilibrating for 30 days, the aqueous and solid phases in the batch sorption reactors were collected by membrane (0.22 μm pore size) filtration.

The total concentration of Se, S, Ca, and Fe in the filtrates was measured by inductively coupled plasma optical emission spectrometry (ICP-OES) with a Varian 720-ES apparatus after dilution with degassed ultrapure water. The distribution ratio (*R_d*) of Se was then calculated (Text S1). By employing the methylene blue method,^{27,28} the total concentration of aqueous S(-II), here called as methylene-blue-detectable sulfur (MBS), in the original filtrates is determined. Sorption products from all of the reactors were stored in a glovebox for the following solid characterization.

2.4. Selenium and Sulfur K-Edge X-Ray Absorption Near-Edge Structure (XANES)–Extended X-Ray Absorption Fine Structure (EXAFS) Spectroscopy. Sulfur K-edge (2474 eV) and selenium K-edge (12 658 eV) XAS experiments were conducted at the XAFS beamline of synchrotron Elettra, Basovizza, Trieste.²⁹ A Si(111) double-crystal monochromator was used with an about 0.3 eV resolution at 2.5 keV. A silicon drift detector (KETEK GmbH AXAS-M with an area of 80 mm²) was employed for collecting the fluorescence signal. For selenium, elemental Se foil was used for energy calibration in parallel. Elemental sulfur standard was measured and then calibrated at the beginning and the end of S K-edge experiments. All of the samples for XAS were sealed using polyimide tape (double-faced sealing for selenium samples, but one-side pasting for sulfur samples), mounted on a sample holder, and measured in fluorescence mode, except for Se references, which were prepared as pellets with cellulose matrix and measured in transmission mode. Before being transferred into the vacuum experimental chamber, the samples were stored under the N₂ atmosphere. For EXAFS signal collection, a liquid N₂ cryostat was used to lower the temperature to 77 K, to minimize the effects of thermal disorder due to atomic vibrations.

Data integration and reduction of X-ray absorption near-edge structure (XANES) spectra (Athena), as well as the data

Table 1. Concentrations of Selected Aqueous Ions and the Retardation Factors in Se(IV) Reactors with an Equilibrium Time of 30 Days, Approximately^a

cement type	matrix	[Ca] _{tot} (mM)	[S] _{tot} (mM)	[Se] _{tot} (mM)	[MBS] (mM)	R _d (L g ⁻¹)
	synthetic CPW	1.230(263)	1.510(14)	0.1789(32)	0.0002(1)	
HCEM-V		0.787(208)	1.470(11)	0.1067(11)	0.0355(8)	0.0676(33)
C-Mag		0.789(201)	1.530(43)	0.1259(18)	0.0291(6)	0.0420(30)
C-Hem		0.747(206)	1.540(16)	0.1192(27)	0.0322(9)	0.0501(37)
C-Goe		0.804(222)	1.450(22)	0.1174(18)	0.0271(6)	0.0524(32)
C-NZVI		0.658(198)	1.620(35)	0.0043(1)	0.0472(9)	4.0346(912)
C-M/H		0.768(213)	1.560(29)	0.1247(19)	0.0335(7)	0.0435(31)
C-M/G		0.781(211)	1.700(9)	0.1296(29)	0.0333(9)	0.0380(35)

^aPrior to introducing Se(IV), each type of hydrated cement equilibrated with CPW for ~48 h. Standard errors are given by the number in brackets on the last digit(s). The Se detection limit with our ICP-OES is 0.1 ppm.

fitting of extended X-ray absorption fine structure (EXAFS) spectra (Artemis)³⁰ were performed using the Demeter software package. A linear combination fit (LCF) was applied to the Se XANES spectra to identify and quantify the selenium species. The *k*³-weighted EXAFS functions of the Se samples and the *k*²-weighted ones of the S samples were Fourier-transformed (FT) in a *k* range of 3.0–13.0 Å⁻¹ using a Kaiser–Bessel window. Theoretical backscattering paths were calculated by FEFF8.4,³¹ to perform the fit in back-transformed reciprocal space (*k*).

2.5. Pair Distribution Function (PDF) Analysis. Se(IV)-reacted Fe⁰ and Fe-(hydr)oxides particles (sorption experiment conditions described in Text S2) were investigated by PDF analysis of X-ray scattering. High-energy X-ray scattering experiments were performed in beamline ID31 at the ESRF, using an energy of 70.0 keV and a PerkinElmer XRD 1621 flat detector. To avoid any oxidation, the reacted NZVI and Fe-(hydr)oxides powder samples were packed in Ø1 mm polyimide capillaries and sealed inside capillaries by epoxy glue in a glovebox. These loaded capillaries were stored in anaerobic conditions until they were put on the sample racks. An NIST-certified CeO₂ powder sample was used for instrumental calibration, and empty capillary with the same specification for background subtraction. With a collection time of 180 s, the obtained images were integrated to one-dimensional diagrams using Fit2D software.³² PdfGetX3 code³³ was employed to transform the data into PDF patterns, and the calculated PDF patterns were obtained by PDFGui software.³⁴

3. RESULTS AND DISCUSSION

3.1. Mineralogical Compositions of Hydrated Cements. The XRD patterns of the synthesized Fe products are shown in Figure S1, with no impurity diffraction peak visible. The crystalline phases in HCEM-V were mainly portlandite, ettringite, AFm-SO₄, calcite, mullite, and quartz, in a good agreement with a previous study.³ The total Fe content of the pure CEM-V/A was determined to be 3.3 wt % Fe oxide composition, which should contain reducing Fe-(hydr)oxides originally from BFS and FA (Text S3 and Figure S2). Besides, an amorphous phase was detected, giving a broad peak at 2θ ~ 13.2°. As interpreted by Claret et al.,³ the amorphous phase was not C–S–H⁵ but could be “proto-C–S–H”. The distinction between C–S–H and the rest of the amorphous/nanocrystalline matrix is seldom made in XRD studies due to their poor crystallinity.³⁵ Apart from this amorphous phase, no visible peak attributed to C–S–H was observed. Regarding the hydrated Fe-bearing CEM-V/A cements, in addition to the

diffraction peaks of hydrated cement itself, the presence of corresponding iron phases also resulted in obvious diffraction peaks. In comparison to the blank hydrated cement, the corresponding amorphous phase in Fe-bearing cements showed a much weaker diffraction signal, indicating that the formation of the amorphous phase was largely inhibited in the presence of the nanosized (Figure S3) iron phases.

3.2. S(-II) Leaching Kinetics and Se(IV) Sorption. The leaching kinetics of total sulfide species ([MBS], including S²⁻, S_n²⁻, and H₂S) from HCEM-V in the synthetic CPW was studied, and the total aqueous concentrations of Ca and S were recorded (Figure S4) as well. After equilibrating with HCEM-V, ~0.4 mM more S was leached into the aqueous phase and ~30% of Ca²⁺ was adsorbed. With equilibrium time increasing, a considerable amount of sulfide leached out from HCEM-V. [MBS] reached the maximum value of 0.15 mM at 144 h. Aqueous sulfide could originate from the blending BFS, and its maximum concentration should be limited by the oxidants existing in HCEM-V, like Fe(III)-(oxyhydr)oxides.

SeO₃²⁻ sorption on HCEM-V particles was investigated by kinetics and batch sorption experiments. Concentration profiles of the kinetic experiment (Figure S5) indicated that total Ca and S concentrations kept almost constant during the reaction time. Besides, [Se]_{tot} decreased rapidly from ~0.18 to ~0.14 mM within 24 h and then continued to decrease slowly even after 700 h. The batch sorption results are shown in Table 1. After the reaction, [Ca]_{tot} and [S]_{tot} in all of the reactors stayed around 0.8 and 1.5 mM, respectively. All of the types of hydrated cement showed a good affinity to SeO₃²⁻, resulting in the R_d values ranging from 0.038 to 4.034 L g⁻¹. C-NZVI showed the strongest affinity and the largest sorption capacity (R_d ~ 4.034 L g⁻¹) toward SeO₃²⁻. As expected, the largest MBS value (0.0472 mM) was determined in the C-NZVI reactor, suggesting that NZVI could protect sulfide from being oxidized. For reactors containing Fe-(oxyhydr)oxides, [MBS] was nearly identical at ~0.03 mM, which was a little lower than the value in the HCEM-V reactor (~0.04 mM).

Se(IV) has the potential to oxidize S(-II) into S(0) and, consequently, to be reductively immobilized. The more reductive condition in the HCEM-V reactor compared to those with extra Fe-(oxyhydr)oxides, as indicated by the higher [MBS] value, could be partially responsible for its larger R_d value of 0.0676 L g⁻¹. Certainly, cement hydration phases (e.g., proto-C–S–H, AFm phase, and ettringite) with different proportions in different Fe-bearing cements should also contribute to the different R_d values, as these hydrates are widely considered as potential phases to remove anionic contaminants via surface adsorption and anion exchange.^{18,36,37}

In addition, comparing with the leaching kinetic experiment of HCEM-V (Figure S4), [MBS] values in batch sorption experiments were generally lower probably due to the introduction of the oxidant of Se(IV). In conclusion, introducing Fe-(oxyhydr)oxides into the hydrated ternary blended cement would not obviously enhance its uptake performance toward SeO_3^{2-} . The lack of reactivity enhancement in the reactors with extra amounts of Fe-(oxyhydr)oxides could be due to the inherent existence of reducing and oxidizing Fe phases in blended cement.^{38,39} The sorbed selenium species were further identified.

3.3. Se Species from Se K-Edge XANES. Sorption products on the seven types of hydrated cement were analyzed by the LCF of Se K-edge XANES spectra (Figure 1). From the

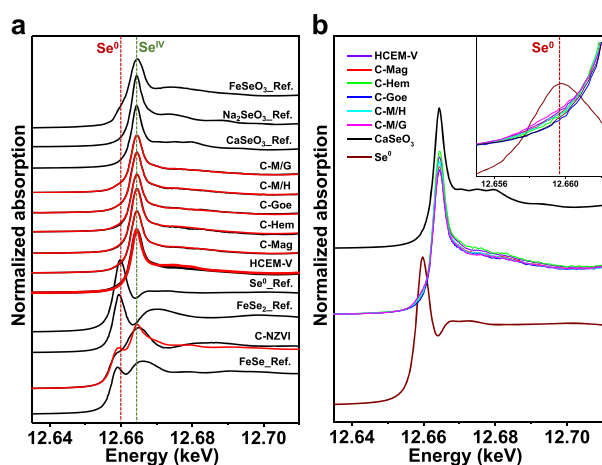


Figure 1. Se K-edge normalized XANES spectra. (a) Spectra of Se(IV) sorbed on hydrated cement with LCF results and the related Se references. (b) Normalized XANES spectra comparison of Se(IV) sorption products and references of red Se^0 and CaSeO_3 , showing the reduction of Se(IV) to Se^0 . The inset shows the extended XANES spectra of cement samples at the energy position of the Se^0 white-line peak.

LCF results listed in Table S2, it is found that the Se(IV) reduction only occurred, to a large extent, on C-NZVI, resulting in 68.1% FeSe and 6.9% Se^0 . Besides, a 20.5% CaSeO_3 contribution was quantified by LCF, probably attributed to the co-precipitation of CaSeO_3 or inner-sphere surface complexes between Ca^{2+} and SeO_3^{2-} . The spectrum of C-NZVI cannot be reproduced perfectly by the three references (Figure 1a), indicating that SeO_3^{2-} could be adsorbed on different hydrated cement products or reduced by secondary phases generated from NZVI. For HCEM-V, Se species were mainly composed of CaSeO_3 and Na_2SeO_3 , suggesting that sorbed SeO_3^{2-} may form inner-sphere complexes (like CaSeO_3) and outer-sphere complexes (i.e., water-coordinated SeO_3^{2-}). For instance, sorbed SeO_3^{2-} on the AFm phase may form outer-sphere complexes, having similar XANES features to Na_2SeO_3 .³⁶ Besides, introducing a tiny amount ($\sim 0.7\%$) of Se^0 minimized the reduced χ^2 value, though this low value falls within the uncertainty range. The HCEM-V spectrum was subsequently used as a reference to perform the LCF analysis of the other cement samples. For the hydrated cement containing Fe-(oxyhydr)oxides, in addition to the largest contribution of HCEM-V reference, small percentages of FeSeO₃ can be added to improve the fits, indicating that SeO_3^{2-} may complex with the Fe phases

added.⁴⁰ Indeed, the tiny amount of Se^0 identified by the LCF analysis was inconclusive in the hydrated cement. However, qualitative observation of their XANES spectra shows changes at the energy position of the Se^0 white-line peak (i.e., the sharp intense peak in the near edge) that can be considered significant.

As shown in the inset of Figure 1b, the absorption intensity at the white-line peak position of Se^0 increased, indicative of the formation of Se^0 . Note that the intensity increase for the blank hydrated cement was even larger than that for cements with the addition of magnetite, e.g., C-Mag and C-M/H. Typically, the effective reductants in the ternary blended cement could be Fe(II)-bearing phases and be sulfide phases.^{38,39,41,42} To reduce Se(IV), these phases could be even more effective than the nanosized magnetite introduced. The specific reductants at work need to be ascertained.

3.4. Se K-Edge EXAFS. EXAFS spectra of samples HCEM-V and C-NZVI were also collected, together with some references, to determine the coordination environments of sorbed selenium. The k^3 -weighted EXAFS oscillations (Figure 2a) showed that the two samples resulted in quite different

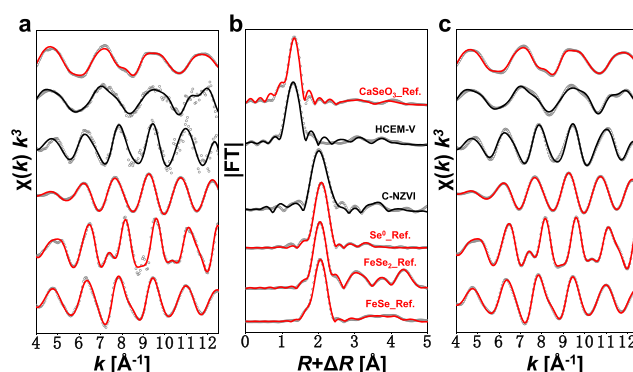


Figure 2. Experimental Se K-edge EXAFS spectra of HCEM-V and C-NZVI samples and reference compounds. (a) k^3 -Weighted EXAFS oscillations. (b) Fourier-transformed (not corrected for phase shift) EXAFS signals. (c) Back-Fourier-transformed EXAFS signal. The gray circles are the experimental data, and the solid lines are fit results.

oscillation frequencies. After Fourier transformation, radial distribution functions (Figure 2b) were obtained showing the presence of multiple neighbor shells. The first neighbor shell of HCEM-V was fitted with three Se–O backscattering pairs at $R = 1.69 \text{ \AA}$, and the further shells could be reproduced by each of the two Se–Ca at $R = 3.29$ and 3.53 \AA (Table S3). This Se complexation environment was similar to that of the CaSeO_3 reference, suggesting that most sorbed SeO_3^{2-} on HCEM-V may co-precipitate with Ca or structurally coordinate with Ca sites of hydrated cement products. In contrast, most Se on C-NZVI was within reducing species, with its first shell fitted with a CN ~ 1.0 Se–Se pair at $R = 2.37 \text{ \AA}$ and a CN ~ 1.4 Se–Fe pair at $R = 2.39 \text{ \AA}$. Besides, a second neighbor shell with a Se–Se backscattering pair generated from the FeSe structure was added, which resulted in an improved fit. Thus, the Se coordination environment in C-NZVI can be described by that of Se^0 and FeSe, in accordance with the species distribution obtained from the XANES data. This fact leads to predicting that the Se removal would be controlled by co-precipitation/incorporation on Ca sites or via a reductive precipitation process, when occurring in the bare hydrated cement phases or close to the embedded steel, respectively.

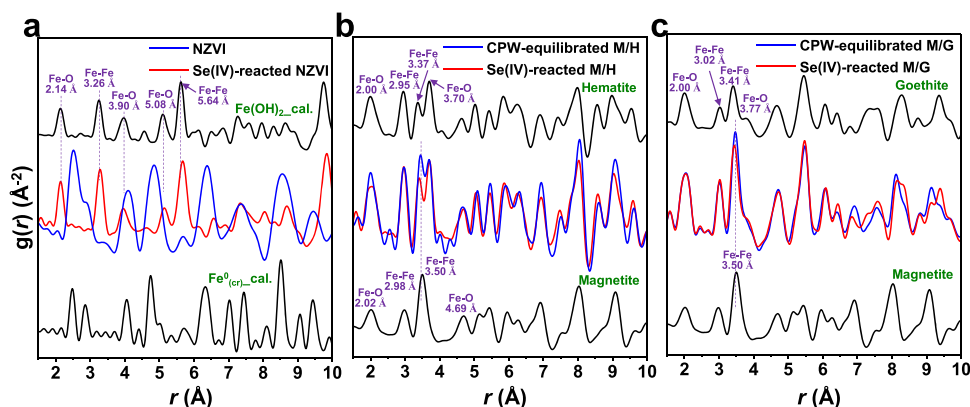


Figure 3. Experimental PDF patterns of Se(IV) sorption products on Fe products (i.e., NZVI, M/H, and M/G) and calculated PDF patterns of the related Fe products. (a) Experimental PDF of pristine NZVI and Se(IV)-reacted NZVI; calculated PDF references of $\text{Fe}^0_{(\text{cr})}$ and $\text{Fe}(\text{OH})_2$. (b) Experimental PDF of magnetite, hematite, M/H couple, and Se(IV)-reacted M/H. (c) Experimental PDF of magnetite, goethite, M/G couple, and Se(IV)-reacted M/G.

3.5. Reducibility of Steel Corrosion Products toward

Se(IV). Steel corrosion products are considered as good scavengers for SeO_3^{2-} . However, based on the above results, their addition to hydrated CEM-V/A cement did not significantly enhance the Se removal. Chemical interactions between steel corrosion products and SeO_3^{2-} in CPW were investigated and compared to the results in the presence of hydrated CEM-V/A cement. After ~ 100 days of reaction, the aqueous concentrations in equilibrium were determined (see Table S4). Comparing to the cement-including cases (Table 1), $[\text{Se}]_{\text{tot}}$ in equilibrium and R_d values in the absence of cement showed only small differences. The solid phases before and after the reaction were studied by PDF analysis. After equilibrating with SeO_3^{2-} , NZVI transformed into $\text{Fe}(\text{OH})_2$ completely due to the oxidation by Se(IV) and H_2O . Regarding M/H (Figure 3b), the correlation at ~ 3.50 Å decreased significantly after the reaction, which corresponds to a decrease in the coordination number of the Fe–Fe scattering pair from magnetite. In the magnetite structure, the bond length of ~ 3.50 Å is the distance between neighboring tetrahedron and octahedron (Figure S6). In the inverse spinel structure of magnetite, all tetrahedral sites are occupied by Fe(III) and octahedral sites are occupied by both Fe(III) and Fe(II). Our results point to the oxidation of Fe(II) sites by Se(IV), leading to a change in the surface structure. A similar phenomenon was observed in the case of M/G (Figure 3c). In addition, the selenium-sorbed species have been investigated in our previous work,²² showing that at least $\sim 50\%$ sorbed Se(IV) was reduced under similar experimental conditions. The study indicated that both Fe(0) and magnetite still showed strong reducing ability toward Se(IV) in hyperalkaline CPW. In contrast, tiny amounts of Se(IV) were reduced in the presence of hydrated cement, although the resulting R_d values were almost the same. This suggests that the redox reactivity of steel corrosion products can be greatly suppressed due to the cement coatings. Besides, the nonredox Se(IV) sorption on Fe phases, weakening their chemical interactions.

3.6. Inherent Sulfur-Reducing Phases in CEM-V/A

Cement. To ascertain the leaching source of reduced sulfur, S K-edge XAS was employed to characterize sulfur species in HCEM-V and C-NZVI. As shown in Figure 4a, their normalized XANES spectra were quite similar, possessing a main absorption peak at the energy position of the sulfate

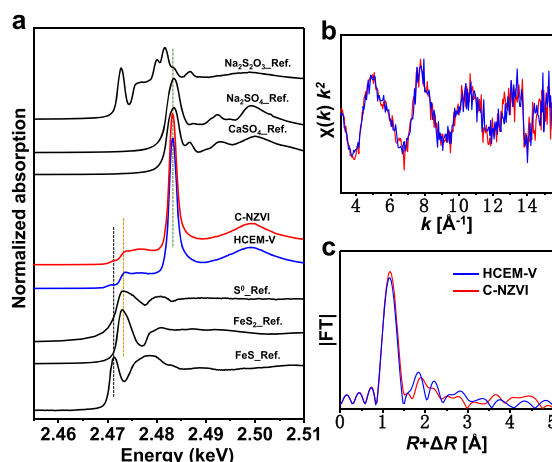


Figure 4. S K-edge XAS spectra. (a) Normalized XANES spectra of HCEM-V, C-NZVI, and related S references. (b) k^2 -Weighted EXAFS oscillations of HCEM-V and C-NZVI. (c) Fourier-transformed (not corrected for phase shift) EXAFS signals.

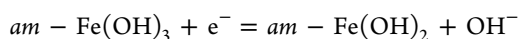
white-line peak. In CEM-V/A cement, most sulfur species have +6 oxidation state, such as S(VI) in gypsum, AFm phase, and ettringite. Besides, at least two small absorption peaks can be observed at lower energies, close to feature peak energies of FeS, FeS_2 , and S^0 . The absorption peak at ~ 2471 eV can be a strong evidence for sulfide minerals. However, due to their small amount and different crystallinities, it was hard to identify the exact sulfide forms, e.g., Fe sulfide or other metal (e.g., Cu and Cd) sulfides. In addition, the very close white-line peak positions of FeS_2 and S^0 increased the difficulty of ascertaining the S species attributions at ~ 2473 eV. Both S(-I) and S(0) species are potentially present in the hydrated cement. The k^2 -weighted EXAFS oscillations and Fourier-transformed EXAFS signals of HCEM-V and C-NZVI are shown in Figure 4b,c. Introducing NZVI did not result in an obvious difference in the sulfur spectra, indicating that Fe(0) cannot promote the formation of more sulfur-reducing species by redox reactions in the hydrated cement system.

The signal oscillation frequency in k space and the signal neighbor shell at $R + \Delta R \sim 1.17$ Å were attributed to the four S–O backscattering pairs ($d \sim 1.48$ Å) from SO_4^{2-} . For the second shells, the backscattering peaks were quite weak as the major sulfur form, SO_4^{2-} , mostly locates in the AFm phase and

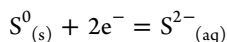
ettringite, in which SO_4^{2-} is loosely bonded in the interlayer and channels, respectively, thus receiving a weak backscattering signal from further neighbor shells.³⁶ Signal contributions from the minor S species were not visible enough in the EXAFS spectra, but these S forms, i.e., sulfides and bisulfides, were critical for Se(IV) reduction.

3.7. Possible Redox Reactions Involving Se, Fe, and S.

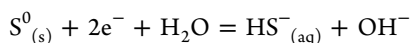
In steel-reinforced concrete made with CEM-V/A cement, reducing Fe phases (from steel reinforcements, BFS, and FA) and sulfides (from BFS) contribute together to the reducing capacity. The distribution of aqueous sulfide species was investigated as a function of pH using CPW as the matrix. As shown in Figure S7, S^{2-} became the predominant species at pH 13.5, which would be the main S(-II) form to participate in redox reactions. ZVI can generate the lowest Eh values and thus possess the strongest reducing ability. However, the active surface of ZVI is often passivated by corrosion layers and cementitious materials, lowering its control over the Eh value that is then dominated by the products of steel corrosion. Our previous study showed that the Eh value in the corroded steel system was controlled by the amorphous $\text{Fe}(\text{OH})_2/\text{Fe}(\text{OH})_3$ couple, resulting in a value of -456 mV at pH 13.5.²² In spite of the active ZVI surface which can even reduce H_2O to $\text{H}_2(\text{g})$, the possible half-reactions involving Fe(II), S(-II), and Se(IV) are



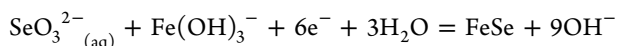
$$\Delta_r G^0 = 46.83 \text{ kJ mol}^{-1} \quad E_h^0 = -486 \text{ mV} \quad (1)$$



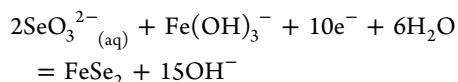
$$\Delta_r G^0 = 109.85 \text{ kJ mol}^{-1} \quad E_h^0 = -569 \text{ mV} \quad (2)$$



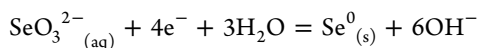
$$\Delta_r G^0 = 92.16 \text{ kJ mol}^{-1} \quad E_h^0 = -478 \text{ mV} \quad (3)$$



$$\Delta_r G^0 = 208.60 \text{ kJ mol}^{-1} \quad E_h^0 = -360 \text{ mV} \quad (4)$$



$$\Delta_r G^0 = 307.88 \text{ kJ mol}^{-1} \quad E_h^0 = -319 \text{ mV} \quad (5)$$



$$\Delta_r G^0 = 130.49 \text{ kJ mol}^{-1} \quad E_h^0 = -338 \text{ mV} \quad (6)$$

The $\Delta_r G^0$ values used are listed in Table S5. For each half-reaction, the Eh values as a function of $[\text{S}^{2-}]_{\text{aq}}$ or $[\text{SeO}_3^{2-}]_{\text{aq}}$ at pH 13.5 were calculated using the Nernst equation

$$E_h = -\frac{\Delta_r G^0}{nF} - \frac{RT}{nF} \ln \frac{a_{\text{red}}}{a_{\text{ox}}} \quad (7)$$

where R and F are the universal gas constant and Faraday constant, respectively, n is the mol number of electrons transferred, a is the chemical activity for the relevant species, and $\Delta_r G^0$ is the standard Gibbs free energy of reaction.

Generally, the oxidation of metal sulfides is controlled by two pathways, thiosulfate and polysulfide pathways.^{16,24} Unlike the thiosulfate pathway (for acid-insoluble pyrite), the polysulfide–elemental sulfur pathway predominates for acid-soluble metal sulfides. As characterized by X-ray diffraction computed tomography (XRD-CT), the slag blended in CEM-V/A is more amorphous and thus contains more acid-soluble metal sulfides.³ In the course of polysulfide oxidation, more than 90% of the sulfide in a metal sulfide can transform to S^0 as well as minor products of thiosulfate, polythionates, and sulfate. The two half-reactions of S^0/S^{2-} and $\text{SeO}_3^{2-}/\text{Se}^0$ were also confirmed with the experimental observation on the reaction between 0.15 mM S(-II) and 0.2 mM Se(IV) in CPW (Figure S8).

The Eh value change as a function of $[\text{S}^{2-}]_{\text{aq}}$, $[\text{HS}^-]_{\text{aq}}$, or $[\text{SeO}_3^{2-}]_{\text{aq}}$ for each half-reaction in CPW is plotted in Figure 5.

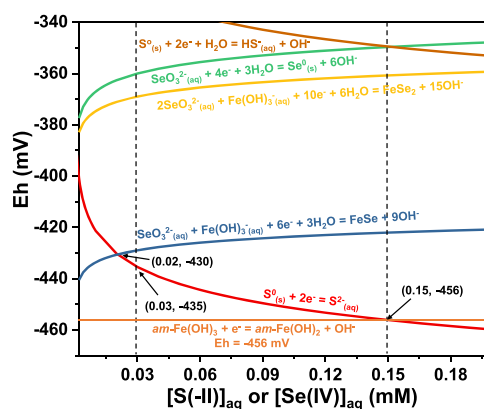


Figure 5. Redox potential change of each selected half-reaction as a function of $[\text{S}(-\text{II})]_{\text{aq}}$ or $[\text{Se}(\text{IV})]_{\text{aq}}$ at pH 13.5. $\text{Fe}(\text{OH})_3^-$ concentration was set as 5 ppb, i.e., 10^{-7} M.

At a fixed pH, the $am\text{-Fe}(\text{OH})_3/am\text{-Fe}(\text{OH})_2$ half-reaction always gives an Eh value of -456 mV, imposed together by all of the Fe phases in the reinforced concrete. The Eh curves of $am\text{-Fe}(\text{OH})_3/am\text{-Fe}(\text{OH})_2$ and S^0/S^{2-} intersected at (0.15, -456), indicating that the dissolved $[\text{S}^{2-}]$ in equilibrium can only reach ~ 0.15 mM at -456 mV. Otherwise, the Eh values imposed by S^0/S^{2-} would be more negative than by $am\text{-Fe}(\text{OH})_3/am\text{-Fe}(\text{OH})_2$, leading to the oxidation of S^{2-} to S^0 . This is in a good agreement with the S(-II) leaching kinetic study (Figure S4), showing that [MBS] reached the top at ~ 0.15 mM. As reported in the literature, much higher $[\text{S}(-\text{II})]_{\text{aq}}$ was released from slags into cement pore solutions, e.g., ~ 80 to ~ 110 mM⁴³ and ~ 10 mM⁴⁴ at pH ~ 12 . Those types of slags contain less than ~ 1.0 wt % Fe_2O_3 , while the slag in CEM-V/A ~ 3.3 wt % Fe_2O_3 .³ The lower $[\text{S}^{2-}]_{\text{aq}}$ in the current study could be due to the higher pH values and larger portions of Fe(III) phases, which originally existed in the supplementary cementitious materials (SCMs) and/or were from Fe(II) oxidations during storage. As a result, the predominant half-reaction of $am\text{-Fe}(\text{OH})_3/am\text{-Fe}(\text{OH})_2$ would limit the maximum $[\text{S}(-\text{II})]_{\text{aq}}$. After adding SeO_3^{2-} , higher Eh values were imposed by the possible half-reactions of $\text{SeO}_3^{2-}/\text{FeSe}$, $\text{SeO}_3^{2-}/\text{FeSe}_2$, and $\text{SeO}_3^{2-}/\text{Se}^0$, leading to a lower $[\text{S}(-\text{II})]_{\text{aq}}$ of ~ 0.03 mM. The $[\text{S}(-\text{II})]_{\text{aq}}$ decrease from ~ 0.15 to ~ 0.03 mM could account for the reductive precipitation of SeO_3^{2-} to Se^0 . However, this is not fully supported by the observation of a tiny amount of Se^0 in XANES spectra (Figure 1) probably as Se^0 colloids were formed (Text S4 and Figure S9) but not fully

collected by the 0.22 μm filter membrane. After a 30-day reaction, $[\text{SeO}_3^{2-}]_{\text{aq}}$ decreased to ~ 0.10 mM, still giving a higher Eh value than the S^0/S^{2-} curve. This indicated that the redox reactions between Se(IV), S(-II), and Fe(II) have not reached equilibrium after 30 days and more Se(IV) should be reduced with a longer reaction time.

3.8. Environmental Implications. Considering that reductive precipitation is one of the critical retardation pathways for redox-sensitive RNs, especially for anionic RNs that are more soluble and thus mobile in alkaline conditions, reinforced cementitious structures designed for underground nuclear waste repositories should retain a reducing capacity. Satisfyingly, hydrated CEM-V/A cement itself shows a certain reducing ability toward SeO_3^{2-} even after a relatively short interaction period (~ 30 days) compared to the geologic time scales. Obviously, cement hydration phases showed the major retention capacity for SeO_3^{2-} and immobilized the RN analogue via nonredox reactions. According to the Se K-edge XANES–EXAFS analyses, Se(IV) formed both inner-sphere (with Ca sites) and outer-sphere complexes with the cement hydrates. We assumed that the nonredox sorption of Se(IV) could be largely determined by the anionic sites (outer surface vs interlayer/interchannel) of the AFm and AFt phases, and the Ca sites of C–S–Hs and portlandite.¹¹ For a longer-term interaction, reductive immobilization would play a more critical role for redox-sensitive RNs. After thousands of years, hydrated PC is expected to degrade into C–S–H gel and aluminoferrite minerals and the pore solution pH to drop to 11 or even lower.⁴⁵ Therefore, more reducing entities, e.g., Fe^{2+} and HS^- , could leach out from the cement and participate in redox reactions.

The chemical role of steel reinforcement was simulated by introducing various Fe-(oxyhydr)oxides, their redox couples, and Fe^0 before cement hydration. Results showed that only Fe^0 can largely promote Se(IV) reduction. Magnetite and Fe couples have almost no effect on the reduction. In contrast, introducing only Fe(III)-(oxyhydr)oxides weakened Se(IV) reduction as the Fe(III) phases could oxidize the stronger sulfide reductants.⁴⁶ This indicates that in the PC–BFS–FA ternary blended cement, the active reducing interfaces could be controlled by the passivated iron, i.e., Fe(II)/Fe(III) interface,²² and by sulfides. Their oxidation–reduction relationship is shown in Figure 5. The resulting redox potential should be weighted by their relative predominance. If sulfides predominate over Fe-(oxyhydr)oxides, a considerable amount of aqueous S(-II) can be released and the Eh could reach a value lower than -456 mV at pH 13.5. Since $\text{am-Fe}(\text{OH})_3$ can limit $[\text{S}^{2-}]_{\text{aq}}$ via oxidation to a very low value, ~ 0.15 mM, we generally consider that the reducing ability is in the order of $\text{Fe}^0 > \text{S}^{2-} > \text{am-Fe}(\text{OH})_3$. Besides, Fe^0 is not able to reduce SO_4^{2-} into a lower-valent sulfur species in CPW, as confirmed by S K-edge EXAFS. The embedment of steel (Fe^0) should increase the total reducing capacity of reinforced cementitious materials, but will be not likely to consequently increase the apparent reducing impact with respect to RNs, as the steel surface is always passivated and then corroded into Fe-(oxyhydr)oxides. Therefore, the reactivity of steel could be weaker compared to that of sulfides that can release soluble S^{2-} .

This work could serve as a guide for cement manufacturing and selection of SCMs applied for nuclear waste repositories in terms of redox potentials. For instance, introducing more (bi)sulfide-rich granulated blast furnace slags in blended

cements and less exposure to the air (e.g., fresh blended cement) can provide a better reducing ability, which should be beneficial for the long-term reductive immobilization of RNs. Besides, the redox and nonredox sorption sites determined here can also give some enlightened hints on the chemical interactions between reinforced concretes (the most widely used construction materials) and their surrounding contaminants.

■ ASSOCIATED CONTENT

Supporting Information

The Supporting Information is available free of charge at <https://pubs.acs.org/doi/10.1021/acs.est.9b06876>.

XRD patterns and FE-SEM micrographs of the synthesized Fe products and hydrated cements; kinetics of HCEM-V dissolution and SeO_3^{2-} sorption on HCEM-V; Se K-edge EXAFS; atomistic structure of magnetite; EPMA image and EDS results of polished HCEM-V cement core; photos of reaction products of aqueous Se(IV) and S(-II); DLS results; CPW content; LCF results; EXAFS refinement; aqueous results of SeO_3^{2-} sorption on Fe phases in N_2 atmosphere; and a list of $\Delta_f G^0$ values used (PDF)

■ AUTHOR INFORMATION

Corresponding Authors

Bin Ma – Univ. Grenoble Alpes, Univ. Savoie Mont Blanc, CNRS, IRD, IFSTTAR, ISTERre, 38000 Grenoble, France; Laboratory for Concrete & Construction Chemistry, Swiss Federal Laboratories for Materials Science and Technology (Empa), 8600 Dübendorf, Switzerland; orcid.org/0000-0002-4493-4644; Phone: +33(0) 7 67 13 83 83; Email: mabinpku@gmail.com

Alejandro Fernandez-Martinez – Univ. Grenoble Alpes, Univ. Savoie Mont Blanc, CNRS, IRD, IFSTTAR, ISTERre, 38000 Grenoble, France; orcid.org/0000-0001-5073-9629; Phone: +33(0) 4 76 63 51 97; Email: alex.fernandez-martinez@univ-grenoble-alpes.fr

Authors

Kaifeng Wang – Univ. Grenoble Alpes, Univ. Savoie Mont Blanc, CNRS, IRD, IFSTTAR, ISTERre, 38000 Grenoble, France; Decommissioning Engineering Technology Center, China Institute of Atomic Energy, 102413 Beijing, China

Benoît Madé – Andra, 92298 Châtenay-Malabry Cedex, France

Pierre Hénocq – Andra, 92298 Châtenay-Malabry Cedex, France

Delphine Tisserand – Univ. Grenoble Alpes, Univ. Savoie Mont Blanc, CNRS, IRD, IFSTTAR, ISTERre, 38000 Grenoble, France

Sarah Bureau – Univ. Grenoble Alpes, Univ. Savoie Mont Blanc, CNRS, IRD, IFSTTAR, ISTERre, 38000 Grenoble, France

Laurent Charlet – Univ. Grenoble Alpes, Univ. Savoie Mont Blanc, CNRS, IRD, IFSTTAR, ISTERre, 38000 Grenoble, France

Complete contact information is available at:

<https://pubs.acs.org/doi/10.1021/acs.est.9b06876>

Notes

The authors declare no competing financial interest.

634 ■ ACKNOWLEDGMENTS

635 Dr. Giuliana Aquilanti is thanked for her assistance during the
636 Se and S K-edge XAS measurements at the XAFS beamline,
637 Elettra. The authors are grateful to Dr. Nathaniel Findling and
638 Dr. Valérie Magnin for performing XRD and EPMA measure-
639 ments. They acknowledge the use of the Analytical Chemistry
640 Platform at ISTerre (OSUG). This work was supported by a
641 grant from the French National Radioactive Waste Manage-
642 ment Agency (Andra), with partial funding from Labex
643 OSUG@2020 [investissements d'avenir; ANR10 LABX56].
644 B.M. also thanks financial support from the China Scholarship
645 Council (CSC). The authors thank the equipex NanoID
646 (ANR-10-EQPX-39) for access to the nanoZS. The synchro-
647 tron facilities ESRF (BM25A-25-01-976 and ID31) are
648 acknowledged for the allocation of beamtime.

649 ■ REFERENCES

650 (1) Wang, L.; Jacques, D.; De Cannière, P. *Effects of an Alkaline*
651 *Plume on the Boom Clay as a Potential Host Formation for Geological*
652 *Disposal of Radioactive Waste*, External Report SCK-CEN-ER-28;
653 SCK-CEN: Belgium, 2010.
654 (2) Kosakowski, G.; Berner, U. The evolution of clay rock/cement
655 interfaces in a cementitious repository for low- and intermediate level
656 radioactive waste. *Phys. Chem. Earth, Parts A/B/C* **2013**, *64*, 65–86.
657 (3) Claret, F.; Grangeon, S.; Loschetter, A.; Tournassat, C.; De Nolf,
658 W.; Harker, N.; Boulahya, F.; Gaboreau, S.; Linard, Y.; Bourbon, X.;
659 Fernandez-Martinez, A.; Wright, J. Deciphering mineralogical changes
660 and carbonation development during hydration and ageing of a
661 consolidated ternary blended cement paste. *IUCrJ* **2018**, *5*, 150–157.
662 (4) Trotignon, L.; Peycelon, H.; Bourbon, X. In *Performance*
663 *Assessment of CEM-I and CEM-V Concrete Engineered Barriers in a*
664 *Clayey Geological Medium*. MIGRATION Conference, France; 2005.
665 (5) Lothenbach, B.; Nonat, A. Calcium silicate hydrates: Solid and
666 liquid phase composition. *Cem. Concr. Res.* **2015**, *78*, 57–70.
667 (6) Matschei, T.; Lothenbach, B.; Glasser, F. P. Thermodynamic
668 properties of Portland cement hydrates in the system $\text{CaO}-\text{Al}_2\text{O}_3-$
669 $\text{SiO}_2-\text{CaSO}_4-\text{CaCO}_3-\text{H}_2\text{O}$. *Cem. Concr. Res.* **2007**, *37*, 1379–1410.
670 (7) Baur, I.; Keller, P.; Mavrocordatos, D.; Wehrli, B.; Johnson, C. A.
671 Dissolution-precipitation behaviour of ettringite, monosulfate, and
672 calcium silicate hydrate. *Cem. Concr. Res.* **2004**, *34*, 341–348.
673 (8) Matschei, T.; Lothenbach, B.; Glasser, F. P. The AFm phase in
674 Portland cement. *Cem. Concr. Res.* **2007**, *37*, 118–130.
675 (9) Aimoz, L.; Wieland, E.; Taviot-Guého, C.; Dähn, R.; Vespa, M.;
676 Churakov, S. V. Structural Insight into Iodide Uptake by AFm Phases.
677 *Environ. Sci. Technol.* **2012**, *46*, 3874–3881.
678 (10) Evans, N. D. M. Binding mechanisms of radionuclides to
679 cement. *Cem. Concr. Res.* **2008**, *38*, 543–553.
680 (11) Ma, B.; Charlet, L.; Fernandez-Martinez, A.; Kang, M.; Madé,
681 B. A review of the retention mechanisms of redox-sensitive
682 radionuclides in multi-barrier systems. *Appl. Geochem.* **2019**, *100*,
683 414–431.
684 (12) Ochs, M.; Mallants, D.; Wang, L. Radionuclide and Metal
685 Sorption on Cement and Concrete. In *Topics in Safety, Risk, Reliability*
686 *and Quality*; Springer, 2016.
687 (13) Jörg, G.; Buhmann, R.; Hollas, S.; Kivel, N.; Kossert, K.; Van
688 Winkel, S.; Gostomski, C. L. V. Preparation of radiochemically pure
689 ^{79}Se and highly precise determination of its half-life. *Appl. Radiat. Isot.*
690 **2010**, *68*, 2339–2351.
691 (14) Grambow, B. Mobile fission and activation products in nuclear
692 waste disposal. *J. Contam. Hydrol.* **2008**, *102*, 180–186.
693 (15) Chen, F. R.; Burns, P. C.; Ewing, R. C. Se-79: Geochemical and
694 crystallo-chemical retardation mechanisms. *J. Nucl. Mater.* **1999**, *275*,
695 81–94.
696 (16) Charlet, L.; Kang, M. L.; Bardelli, F.; Kirsch, R.; Géhin, A.;
697 Grenèche, J. M.; Chen, F. Nanocomposite pyrite-greigite reactivity
698 toward Se(IV)/Se(VI). *Environ. Sci. Technol.* **2012**, *46*, 4869–4876.

(17) Wu, Y.; Chi, Y.; Bai, H.; Qian, G.; Cao, Y.; Zhou, J.; Xu, Y.; Liu, 699
Q.; Xu, Z. P.; Qiao, S. Effective removal of selenate from aqueous 700
solutions by the Friedel phase. *J. Hazard. Mater.* **2010**, *176*, 193–198. 701
(18) Baur, I.; Johnson, C. A. Sorption of selenite and selenate to 702
cement minerals. *Environ. Sci. Technol.* **2003**, *37*, 3442–3447. 703
(19) Bonhoure, I.; Baur, I.; Wieland, E.; Johnson, C. A.; Scheidegger, 704
A. M. Uptake of Se(IV/VI) oxyanions by hardened cement paste and 705
cement minerals: An X-ray absorption spectroscopy study. *Cem.* 706
Concr. Res. **2006**, *36*, 91–98. 707
(20) Antunes, R. A.; Costa, I.; de Faria, D. L. A. Characterization of 708
corrosion products formed on steels in the first months of 709
atmospheric exposure. *Mater. Res.* **2003**, *6*, 403–408. 710
(21) Fernández-Martínez, A.; Charlet, L. Selenium environmental 711
cycling and bioavailability: a structural chemist point of view. *Rev.* 712
Environ. Sci. Bio/Technol. **2009**, *8*, 81–110. 713
(22) Ma, B.; Fernandez-Martinez, A.; Madé, B.; Findling, N.; 714
Markelova, E.; Salas-Colera, E.; Maffei, T. G. G.; Lewis, A. R.; 715
Tisserand, D.; Bureau, S.; Charlet, L. XANES-based determination of 716
redox potentials imposed by steel corrosion products in cement-based 717
media. *Environ. Sci. Technol.* **2018**, *52*, 11931–11940. 718
(23) Kang, M.; Chen, F.; Wu, S.; Yang, Y.; Bruggeman, C.; Charlet, 719
L. Effect of pH on aqueous Se(IV) reduction by pyrite. *Environ. Sci.* 720
Technol. **2011**, *45*, 2704–2710. 721
(24) Ma, B.; Kang, M.; Zheng, Z.; Chen, F.; Xie, J.; Charlet, L.; Liu, 722
C. The reductive immobilization of aqueous Se(IV) by natural 723
pyrrhotite. *J. Hazard. Mater.* **2014**, *276*, 422–432. 724
(25) Kang, M.; Bardelli, F.; Ma, B.; Charlet, L.; Chen, F.; Yang, Y. 725
The influence of pH and reaction time on the formation of FeSe_2 726
upon selenite reduction by nano-sized pyrite-greigite. *Radiochim. Acta* 727
2016, *104*, 649–656. 728
(26) Scheinost, A. C.; Kirsch, R.; Banerjee, D.; Fernandez-Martinez, 729
A.; Zaenker, H.; Funke, H.; Charlet, L. X-ray absorption and 730
photoelectron spectroscopy investigation of selenite reduction by Fe^{II} - 731
bearing minerals. *J. Contam. Hydrol.* **2008**, *102*, 228–245. 732
(27) Wan, M.; Shchukarev, A.; Lohmayer, R.; Planer-Friedrich, B.; 733
Peiffer, S. Occurrence of surface polysulfides during the interaction 734
between ferric (hydr)oxides and aqueous sulfide. *Environ. Sci. Technol.* 735
2014, *48*, 5076–5084. 736
(28) Mylon, S. E.; Benoit, G. Subnanomolar detection of acid-labile 737
sulfides by the classical methylene blue method coupled to HPLC. 738
Environ. Sci. Technol. **2001**, *35*, 4544–4548. 739
(29) Aquilanti, G.; Giorgetti, M.; Dominko, R.; Stievano, L.; Arčon, 740
I.; Novello, N.; Olivi, L. Operando characterization of batteries using 741
X-ray absorption spectroscopy: Advances at the beamline XAFS at 742
synchrotron Elettra. *J. Phys. D: Appl. Phys.* **2017**, *50*, No. 074001. 743
(30) Ravel, B.; Newville, M. ATHENA, ARTEMIS, HEPHAESTUS: 744
data analysis for X-ray absorption spectroscopy using IFEFFIT. *J.* 745
Synchrotron Radiat. **2005**, *12*, 537–541. 746
(31) Ankudinov, A.; Nesvizhskii, A.; Rehr, J. Dynamic screening 747
effects in X-ray absorption spectra. *Phys. Rev. B* **2003**, *67*, No. 115120. 748
(32) Hammarsley, A. P.; Svensson, S. O.; Hanfland, M.; Fitch, A. N.; 749
Hausermann, D. Two-dimensional detector software: From real 750
detector to idealised image or two-theta scan. *High Pressure Res.* **1996**, 751
14, 235–248. 752
(33) Juhás, P.; Davis, T.; Farrow, C. L.; Billinge, S. J. L. PDFgetX3: a 753
rapid and highly automatable program for processing powder 754
diffraction data into total scattering pair distribution functions. *J.* 755
Appl. Crystallogr. **2013**, *46*, 560–566. 756
(34) Farrow, C.; Juhas, P.; Liu, J.; Bryndin, D.; Božin, E.; Bloch, J.; 757
Proffen, T.; Billinge, S. PDFfit2 and PDFgui: computer programs for 758
studying nanostructure in crystals. *J. Phys.: Condens. Matter* **2007**, *19*, 759
No. 335219. 760
(35) Scrivener, K. L.; Füllmann, T.; Gallucci, E.; Walenta, G.; 761
Bermejo, E. Quantitative study of Portland cement hydration by X-ray 762
diffraction/Rietveld analysis and independent methods. *Cem. Concr.* 763
Res. **2004**, *34*, 1541–1547. 764
(36) Ma, B.; Fernandez-Martinez, A.; Grangeon, S.; Tournassat, C.; 765
Findling, N.; Carrero, S.; Tisserand, D.; Bureau, S.; Elkaïm, E.; Marini, 766
C.; Aquilanti, G.; Koishi, A.; Marty, N. C. M.; Charlet, L. Selenite 767

- uptake by Ca–Al LDH: A description of intercalated anion coordination geometries. *Environ. Sci. Technol.* **2018**, *52*, 1624–1632.
- (37) Ma, B.; Fernandez-Martinez, A.; Grangeon, S.; Tournassat, C.; Findling, N.; Claret, F.; Koishi, A.; Marty, N. C. M.; Tisserand, D.; Bureau, S.; Salas-Colera, E.; Elkaïm, E.; Marini, C.; Charlet, L. Evidence of multiple sorption modes in layered double hydroxides using Mo ss structural probe. *Environ. Sci. Technol.* **2017**, *51*, 5531–5540.
- (38) Simon, S.; Gluth, G. J. G.; Peys, A.; Onisei, S.; Banerjee, D.; Pontikes, Y. The fate of iron during the alkali-activation of synthetic (CaO-)FeO_x-SiO₂ slags: An Fe K-edge XANES study. *J. Am. Ceram. Soc.* **2018**, *101*, 2107–2118.
- (39) Peys, A.; White, C. E.; Olds, D.; Rahier, H.; Blanpain, B.; Pontikes, Y. Molecular structure of CaO–FeO_x–SiO₂ glassy slags and resultant inorganic polymer binders. *J. Am. Ceram. Soc.* **2018**, *101*, 5846–5857.
- (40) Charlet, L.; Scheinost, A. C.; Tournassat, C.; Greneche, J. M.; Géhin, A.; Fernández-Martínez, A.; Coudert, S.; Tisserand, D.; Brendle, J. Electron transfer at the mineral/water interface: Selenium reduction by ferrous iron sorbed on clay. *Geochim. Cosmochim. Acta* **2007**, *71*, 5731–5749.
- (41) Valeev, D.; Mikhailova, A.; Atmadzhidi, A. Kinetics of iron extraction from coal fly ash by hydrochloric acid leaching. *Metals* **2018**, *8*, No. 533.
- (42) Chen, H.; Laskin, A.; Baltrusaitis, J.; Gorski, C. A.; Scherer, M. M.; Grassian, V. H. Coal fly ash as a source of iron in atmospheric dust. *Environ. Sci. Technol.* **2012**, *46*, 2112–2120.
- (43) Gruskovnjak, A.; Lothenbach, B.; Winnefeld, F.; Figi, R.; Ko, S. C.; Adler, M.; Mäder, U. Hydration mechanisms of super sulphated slag cement. *Cem. Concr. Res.* **2008**, *38*, 983–992.
- (44) Lothenbach, B.; Le Saout, G.; Ben Haha, M.; Figi, R.; Wieland, E. Hydration of a low-alkali CEM III/B–SiO₂ cement (LAC). *Cem. Concr. Res.* **2012**, *42*, 410–423.
- (45) Lothenbach, B.; Bernard, E.; Mäder, U. Zeolite formation in the presence of cement hydrates and albite. *Phys. Chem. Earth, Parts A/B/C* **2017**, *99*, 77–94.
- (46) Dos Santos Afonso, M.; Stumm, W. Reductive dissolution of iron(III) (hydr)oxides by hydrogen sulfide. *Langmuir* **1992**, *8*, 1671–1675.